Macromolecules

ARTICLE

pubs.acs.org/Macromolecules

Monte Carlo Phase Diagram for a Polydisperse Diblock Copolymer Melt

T. M. Beardsley* and M. W. Matsen*

School of Mathematical and Physical Sciences, University of Reading, Whiteknights, Reading RG6 6AX, U.K.

ABSTRACT: The phase diagram for an AB diblock copolymer melt with polydisperse A blocks and monodisperse B blocks is evaluated using lattice-based Monte Carlo simulations. Experiments on this system have shown that the A-block polydispersity shifts the order−order transitions (OOTs) toward higher A-monomer content, while the order−disorder transition (ODT) moves toward higher temperatures when the A blocks form the minority domains and lower temperatures when the A blocks form the matrix. Although self-consistent field theory (SCFT) correctly accounts for the change in the OOTs, it incorrectly predicts the ODT to shift toward higher temperatures at all diblock copolymer compositions. In contrast, our simulations predict the correct shifts for both the OOTs and the ODT. This implies that polydispersity amplifies the fluctuation-induced correction to the mean-field ODT, which we attribute to a reduction in packing frustration. Consistent with this explanation, polydispersity is found to enhance the stability of the perforated-lamellar phase.

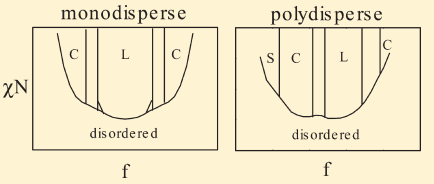

INTRODUCTION

Block copolymer molecules have received considerable attention due to their intriguing behavior and potential applications.[1] The majority of research has focused on the ideal monodisperse AB diblock copolymer system, where all the polymers are identical with N_A A-type monomers joined to N_B B-type monomers, giving a total polymerization of $N = N_A + N_B$ and a composition of $f = N_A/N$. When the interaction between the A and B monomers is sufficiently unfavorable as measured by the Flory−Huggins χ parameter, the diblock copolymers self-assemble into periodically ordered structures with nanometer-sized domains. The equilibrium phase diagram[2] is comprised of the classical lamellar (L), cylindrical (C), and spherical (S) phases as well as a complex gyroid (G) phase.[4,3] Another complex perforated-lamellar (PL) phase is often observed in experiments,[5] but it is understood to be metastable relative to the G phase.[6] A third complex phase with *Fddd* symmetry has also been reported recently,[7] but its region of stability in the phase diagram appears to be very small.

There has been a long-held opinion that the formation of well-ordered morphologies requires the block copolymers to be synthesized via anionic polymerization so as to limit the level of polydispersity.[8] However, experimentalists have begun to realize that this is not necessarily the case,[8,9] implying that it may be acceptable to synthesize the block copolymers via less costly methods. This has inspired efforts to better understand how the phase behavior of block copolymers is affected by elevated degrees of polydispersity. The model system for much of the experimental work[10−14] has been AB diblocks with polydisperse A blocks and monodisperse B blocks.

In most respects, self-consistent field theory (SCFT) has managed to successfully explain the experiments.[15−18] This builds upon the usual explanations of block copolymer behavior, where the entropic stretching energy of the A and B blocks competes with the A/B interfacial energy.[19,20] Because polydisperse blocks are able to fill space more efficiently, the stretching energy of the A domains is reduced which, in turn, predicts an increase in domain size[15−17] as observed in experiments.[10,11,21,22] Furthermore, the reduction in stretching energy of the polydisperse domain changes the preferred curvature of the A/B interface, causing the order−order transitions (OOTs) to shift toward compositions higher in the polydisperse component,[15,16,18] and this too has been seen in experiments.[11−14] Because of the fact that polydisperse melts are multicomponent systems, thermodynamics requires the emergence of two-phase coexistence regions along the phase boundaries,[18] and indeed a number of experimental studies have reported this.[9,10,21,22] However, SCFT and experiments are not consistent with regards to the effect of polydispersity on the order−disorder transition (ODT). Experiments by Lynd and Hillmyer[12] found that $(\chi N)_{ODT}$ is reduced when the minority component is polydisperse and raised when the majority component is polydisperse. SCFT predicts instead that polydispersity lowers $(\chi N)_{ODT}$ at all diblock copolymer compositions.[15,16,18]

In an earlier study,[23] we used Monte Carlo simulations to investigate this inconsistency between SCFT and experiment. The simulations were performed over a range of A-block polydispersity indexes, $PDI_A \equiv (N_A)_w/(N_A)_n = 1.0-2.0$, at an average polymerization of $N \equiv (N_A)_n + N_B = 30$ and a symmetric composition of $f \equiv (N_A)_n/N = 0.5$. In each case, the ODT was bracketed by a hysteresis loop formed by running sequential temperature scans back and forth across the ODT, as first implemented by Vassiliev and Matsen[24] for monodisperse melts. The simulations found no shift in the ODT with increasing polydispersity, which is consistent with the experiments. However, the Monte Carlo study was restricted to a

Received: April 27, 2011
Revised: June 13, 2011
Published: June 30, 2011

single composition, and its ability to locate the ODT was limited by the finite size of the hysteresis loops.

Here we extend our previous Monte Carlo study to a wide range of compositions, f, for polydisperse diblock copolymers of $PDI_A = 1.5$ and $N = 30$. This will allow us to deduce the effect of polydispersity by comparing to an earlier study[25] on monodisperse melts of the same polymerization. To improve the sensitivity of our new study, this time we implement the same parallel tempering procedure used in the monodisperse study. By simulating the different temperatures simultaneously on a multiprocessor platform, we are able to perform far more Monte Carlo steps (MCS) than by the sequential temperature sweeps of our earlier study.[23] Furthermore, the exchange of configurations between adjacent temperatures provides an effective way of overcoming energy barriers allowing equilibrium to be reached more quickly. As a result of the improved statistics, the system generally exhibits a well-defined spike in the heat capacity, C_V, which locates the ODT with far more accuracy than the previous hysteresis loops. In the few cases where there is no discernible spike, we locate the ODT by the disappearance of peaks in the ordered-state scattering function, $S(\mathbf{q})$.

MONTE CARLO ALGORITHM

The current study employs the same lattice model described in detail by Vassiliev and Matsen[24] for monodisperse melts and extended by Beardsley and Matsen[23] to polydisperse melts. It contains $n = \Sigma n_{N_A}$ diblock copolymers, of which n_{N_A} have N_A monomers in their A block, giving a number-averaged polymerization of $(N_A)_n = \Sigma N_A n_{N_A}/n$. The monodisperse B blocks are each composed of N_B monomers. The resulting polymer chains are placed on a lattice with no more than one monomer per lattice site and with bonded monomers occupying nearest-neighbor sites. In order to minimize lattice effects, the model uses a face-centered cubic (fcc) lattice with a large coordination number of $z = 12$ and periodic boundaries. It is constructed by taking an $L \times L \times L$ simple cubic lattice with lattice constant, d, and deleting every second site, producing an fcc lattice with $V = L^3/2$ sites and a nearest-neighbor distance of $b = \sqrt{2}d$. As in our previous study, the default box size is $L = 54$, but nevertheless we often run simulations over a range of sizes in order to assess finite-size effects. To allow room for the polymers to move, the lattice is only filled to a copolymer occupancy of $\varphi_c \equiv nN/V \approx 0.8$. Molecular interactions are limited to neighboring A and B monomers with an interaction strength of ε_{AB}, from which we define a lattice-based Flory–Huggins parameter

$$\chi \equiv \frac{z\varepsilon_{AB}}{k_B T} \tag{1}$$

The simulations are performed in the canonical ensemble by applying the standard Metropolis algorithm over a range of temperatures, $\{\chi_i\}$. At each temperature, the algorithm chooses among four types of Monte Carlo step (MCS): the slithering snake, chain reversal, crankshaft, and block exchange with relative frequencies of 6:1:2:1. Instead of simulating the temperatures sequentially as before,[23] they are now simulated simultaneously on separate CPUs using parallel tempering[26−28] as implemented in our previous monodisperse study.[25] This is done with the introduction of a global move, which attempts to swap the configurations of a randomly selected pair of neighboring temperatures, every 10^3 MCS per monomer.

For given values of L, $(N_A)_n$, and N_B, a simulation begins by equilibrating an athermal configuration (i.e., $\chi = 0$) with 10^6 MCS per monomer, which serves as our initial configuration for finite χ. A sequence of χ_i values ($i = 1, 2, ..., M$) is then selected to span the expected location of the ODT and generally involves $M = 20$ replicas with a spacing of $\Delta\chi N = 0.5$ for compositions exhibiting the strongest transitions and $\Delta\chi N = 1.0$ for most other compositions. The M replicas are all started from the athermal configuration and equilibrated for typically 3×10^6 MCS per monomer, after which the resulting configurations are visually inspected. If the ODT does not appear to have been captured, then the series of temperatures is adjusted and additional relaxation steps are performed. Furthermore, if the acceptance rate of replica exchange between any two neighboring temperatures drops below 20%, then an intermediate temperature point is inserted.

Once the system has been equilibrated, various thermodynamic quantities are independently sampled in each replica, every 40 MCS per monomer. The estimation period usually lasts for about 5×10^6 MCS per monomer. The main quantity of interest is the heat capacity

$$C_V = \frac{{\varepsilon_{AB}}^2}{k_B T^2}\left(\langle {n_{AB}}^2\rangle - \langle n_{AB}\rangle^2\right) \tag{2}$$

where n_{AB} is the total number of A−B monomer contacts and the angle brackets denote Monte Carlo averages. The heat capacity is commonly used to detect first-order transitions,[29] where there is a jump in the internal energy, $\varepsilon_{AB} n_{AB}$. At a transition, the system spends equal amounts of time in the two competing states, causing the internal energy to fluctuate and thus producing a large value of C_V. Moving away from the transition causes one phase to dominate the other, which reduces the fluctuations leading to a drop in C_V. This results in a peak with a width inversely proportional to the difference in internal energy and a height proportional to the difference squared. Thus, the peak becomes sharper and more pronounce as the system size is increased, since $\langle n_{AB}\rangle \propto V$.

However, even when using the largest system size we are able to equilibrate, the transformation from the disordered state to an ordered phase does not always result in a sufficient decrease in $\langle n_{AB}\rangle$ to produce a discernible peak in C_V. Even still, there is usually a significant change in morphology, which can be readily identified by visual inspection of the configurations. However, this is a rather tedious way of locating the ODT. A more convenient alternative is to use the structure function

$$S(\mathbf{q}) = \frac{1}{V}\langle |\sum_{j=1}^{V} \sigma_j \, exp(i\mathbf{q}\cdot\mathbf{r}_j)|^2\rangle \tag{3}$$

where $\mathbf{r}_j$ is the position of the jth lattice site and $\sigma_j = 1$, 0, or -1 if it is occupied by an A-monomer, a vacancy, or a B-monomer, respectively. The ordered phase is then detected by spikes in $S(\mathbf{q})$ produced by the periodicity of the morphology. For simplicity, we generally look at the spherically averaged structure function, $S(q)$, but in some cases we do examine the full function in 3-D reciprocal space for further information.

The shape of the molecular-weight distribution will have some effect on the behavior of the polydisperse melt,[13,30] but we ignore this issue and adopt the usual Schultz–Zimm distribution[31,32]

$$p(N_A) = \frac{k^k N_A^{k-1}}{(N_A)_n^k \Gamma(k)} \, exp\left(-\frac{kN_A}{(N_A)_n}\right) \tag{4}$$

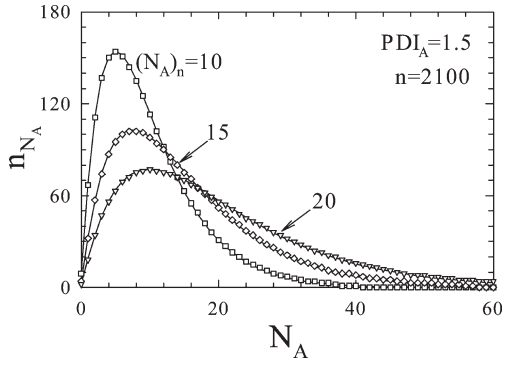

Figure 1. Discrete molecular-weight distributions, $\{n_{N_A}\}$, for a system of $n = 2100$ diblocks with an A-block polydispersity of $PDI_A = 1.5$ and various average polymerizations, $(N_A)_n$. The solid curves compare $np(N_A)$ from the continuous Schultz−Zimm distribution in eq 4.

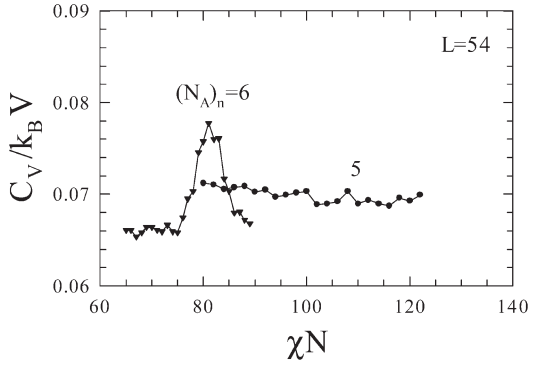

Figure 2. Heat capacity, C_V, plotted as a function of segregation, χN, for compositions adopting a spherical (S) morphology. There is a spike for $(N_A)_n = 6$ signifying an ODT, but not for $(N_A)_n = 5$.

where $PDI_A \equiv (N_A)_w/(N_A)_n = (k + 1)/k$. However, this continuous distribution needs to be converted to a discrete distribution $\{n_{N_A}\}$ with $n = \Sigma n_{N_A}$ total chains and a specified number-averaged polymerization of $(N_A)_n = \Sigma N_A n_{N_A}/n$. For a detailed description of the discretization procedure, we refer the reader to our previous paper.[23] Figure 1 compares the resulting discrete distribution to the continuous distribution, eq 4, for $PDI_A = 1.5$ with $(N_A)_n = 10$, 15, and 20. This example is for $n = 2100$, which corresponds to the number of polymer chains in our default simulation box of $L = 54$.

RESULTS

To facilitate direct comparison to the early study on monodisperse diblocks,[25] we fix the degree of polymerization to the same value, $N = (N_A)_n + N_B = 30$, and sweep across a range of compositions, $(N_A)_n = 4-25$, locating the ODT and identifying the symmetry of the ordered morphology. Based on our previous experience,[23] large polydispersities lead to a variety of computational challenges. For instance, broad molecular weight distributions result in a number of long molecules, particularly for large $(N_A)_n$, which are slow to relax requiring increased equilibration periods. Polydispersity also reduces the tendency of the system to order, making the ODT more difficult to detect. Furthermore, polydispersity creates larger domains and thus generally requires bigger simulation boxes. Therefore, we select an intermediate value of polydispersity, $PDI_A = (N_A)_w/(N_A)_n = 1.5$, that is large enough to have a significant effect, but not too large to create computational difficulties.

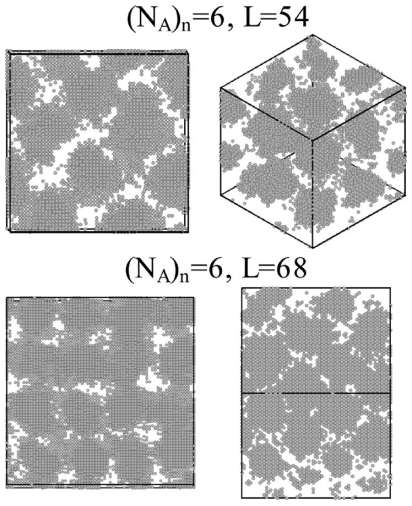

Figure 3. Different orientations of the simulation box showing the minority A-rich spherical (S) domains at $(N_A)_n = 6$ with bcc ($L = 54$ and $\chi N = 87$) and fcc ($L = 68$ and $\chi N = 85$) packing.

Sphere Phase with Monodisperse Matrix. The lowest diblock compositions, $(N_A)_n = 4-6$, formed spherical A-rich domains, but it proved difficult to locate the ODT via the heat capacity, C_V, plotted in Figure 2. While a small spike occurred at $\chi N = 81$ for $(N_A)_n = 6$, no spikes were detected for $(N_A)_n = 4$ and 5. Visual inspection of the ordered configurations at $(N_A)_n = 6$ revealed 8 unit cells of bcc spheres, as depicted in Figure 3a for $\chi N = 87$. The spheres at the other two compositions did appear to order, but with a more complicated packing arrangement.

Further confirmation of the bcc packing for $(N_A)_n = 6$ comes from the spherically averaged structure function, $S(q)$, shown in Figure 4a. Despite a missing $\sqrt{6}$ peak, the indexed reflections are fully consistent with bcc packing. In particular, $S(q)$ has 12 reflections contributing to the principal $\sqrt{2}$ peak, with all their relative angles matching the bcc symmetry. These 12 reflections remain for the $(N_A)_n = 4$ and 5 compositions, but their positions shift to slightly larger wavevectors. More specifically, 8 of the wavevectors increase in magnitude by a factor of $(9/8)^{1/2}$ while the other 4 increase by a factor of $(5/4)^{1/2}$, which then disturbs the relative angles between the reflections and causes a slight splitting of the principal peak. Evidently, the default box size is somewhat too large for 8 unit cells of bcc spheres, and so the bcc packing becomes distorted.

In any case, the formation of bcc spheres contradicts the SCFT prediction[18] that polydispersity stabilizes close-packed arrangements. Working on the assumption that the $L = 54$ simulation box happens to be about the correct size for 8 bcc unit cells (16 spheres), we reduced the volume of the box by about a factor of 4 in hopes of forming one fcc unit cell (4 spheres). For each composition, a number of replicas were equilibrated for box sizes of $L = 30$, 32, and 34, which were then periodically replicated to fill larger boxes of $L = 60$, 64, and 68. After an additional equilibration period of 10^6 MCS per monomer, visual inspection of the larger configurations appeared to show fcc spheres at all three compositions. Figure 3b displays an ordered configuration at $(N_A)_n = 6$ and $\chi N = 85$ from the $L = 68$ box. Indeed, the scattering function, $S(q)$, plotted in Figure 4b is perfectly consistent with fcc symmetry, albeit with the absence of

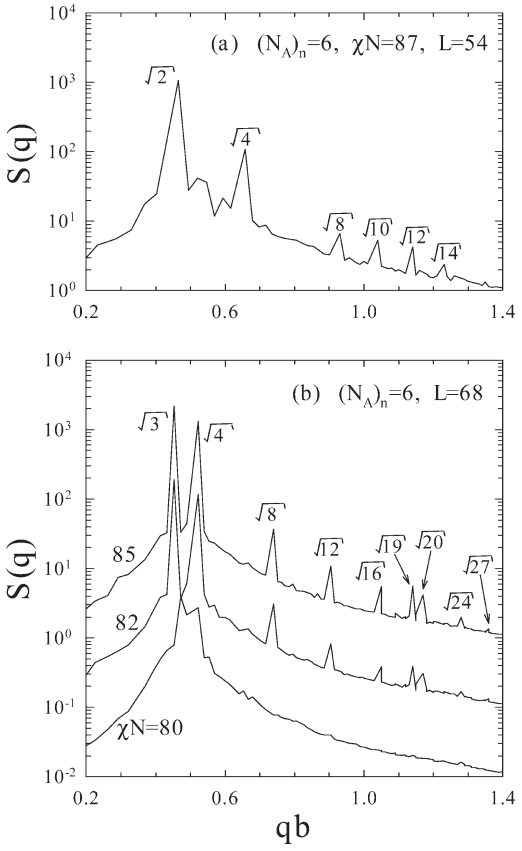

Figure 4. Spherically averaged structure function, $S(q)$, confirming the (a) bcc and (b) fcc packing in Figure 3. The latter plot shows the disappearance of the peaks with decreasing χN; for clarity, the bottom two curves have been shifted downward by 1 and 2 decades.

a $\sqrt{11}$ peak; similar results were obtained for the two lower compositions.

Because of the lack of definitive spikes in the heat capacity, we resorted to a different strategy for locating the ODT.[25] This was done by equilibrating the ordered fcc configurations with 2×10^6 MCS per monomer at a series of temperatures (without parallel tempering swaps) and then evaluating $S(q)$ with a further 10^5 MCS per monomer. The ODT was then identified by the disappearance of the fcc reflections in $S(q)$, as demonstrated in Figure 4. Not surprisingly, the disappearance of the reflections happen at slightly different values of χN for the three box sizes. The lowest value presumably occurs when the box size is commensurate with the preferred size of the fcc unit cell, and so we take this as the relevant $(\chi N)_{ODT}$. Accordingly, our best estimates of the ODT are $(\chi N)_{ODT}$ = 120, 92, and 81 for $(N_A)_n$ = 4, 5, and 6, which were obtained with L = 60, 64, and 68, respectively. Interestingly, the ODT for the fcc spheres at $(N_A)_n$ = 6 matches the location of the heat capacity spike observed for the bcc spheres in the L = 54 simulation box.

Cylinder Phase with Monodisperse Matrix. We were unable to identify an ordered phase for $(N_A)_n$ = 7. Visual inspection of the configurations suggested that the system struggles to select between the spherical (S) and cylindrical (C) morphologies, presumably because the composition is so close to the S/C phase boundary. However, the compositions of $(N_A)_n$ = 8−12 all produced ordered cylinders (C). Unlike for the spheres, the formation of cylinders produced distinct spikes in the heat

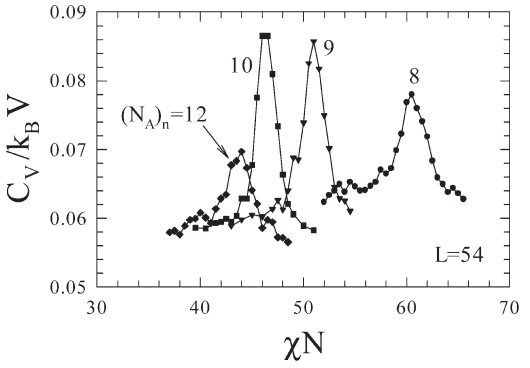

Figure 5. Heat capacity plots analogous to those in Figure 2, but for compositions exhibiting an ordered cylindrical (C) phase.

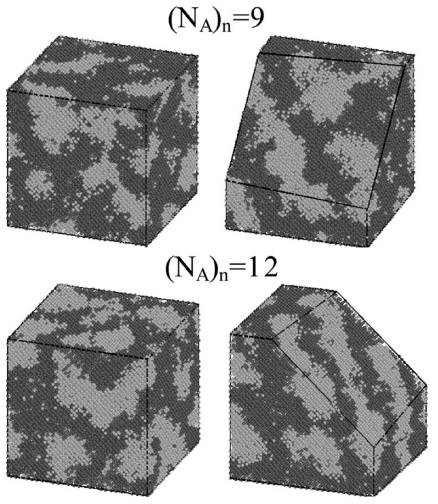

Figure 6. Disordered and ordered configurations adjacent to the ODT at $(N_A)_n$ = 9 (χN = 50.5 and 51.5) and $(N_A)_n$ = 12 (χN = 43 and 44). The simulation boxes of the ordered phase have been clipped so as to reveal the cylindrical (C) morphology.

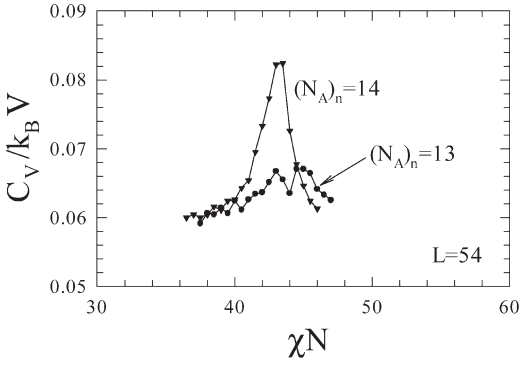

Figure 7. Heat capacity plots analogous to those in Figure 2, but for simulations exhibiting an ordered perforated-lamellar (PL) phase.

capacity as shown in Figure 5. For the purpose of clarity, the curve for $(N_A)_n$ = 11 has been omitted because it closely coincides with those for $(N_A)_n$ = 10 and 12. Notably, the spikes in C_V are relatively small, roughly a third of the size of those produced by monodisperse cylinders.[25] Nevertheless, the transition is clearly first order given that the configurations adjacent to the ODT

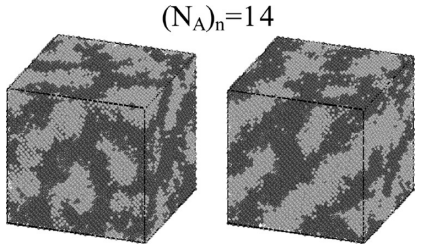

Figure 8. Configurations adjacent to the ODT (χN = 42.5 and 43) at the composition $(N_A)_n$ = 14 demonstrating a transition to perforated lamellae (PL).

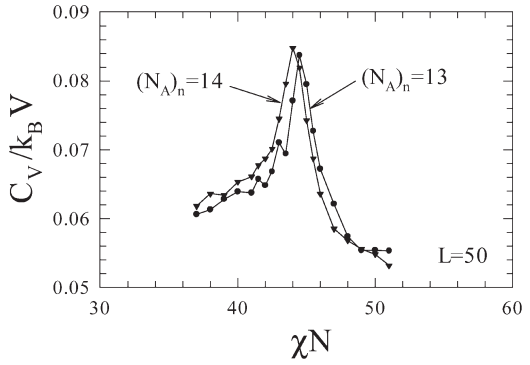

Figure 9. Heat capacity plots analogous to those in Figure 2, but for simulations exhibiting an ordered gyroid (G) phase.

exhibit an abrupt change in morphology, as demonstrated in Figure 6 for $(N_A)_n$ = 9 and 12. Note that the simulation boxes containing the ordered phase have been clipped in order to reveal the internal structure. Although the morphology is obviously that of the C phase, it is not as well formed as in the monodisperse system.[25] This fact combined with reduced size of the spikes in the heat capacity supports our earlier finding[23] that polydispersity reduces the abruptness of the ODT.

Perforated-Lamellar Phase with Monodisperse Matrix. The perforated-lamellar (PL) phase formed in the default box size at both $(N_A)_n$ = 13 and 14, but the behavior was distinctly different. The heat capacity plotted in Figure 7 shows a clear spike for $(N_A)_n$ = 14, whereas there is no visible spike for $(N_A)_n$ = 13. Indeed, the $(N_A)_n$ = 14 configurations displayed an abrupt change in morphology characteristic of a first-order transition, as illustrated in Figure 8. On the other hand, the $(N_A)_n$ = 13 configurations were consistently less well formed and showed no definitive onset of long-range order.

The PL phase also failed to produce a spike in the heat capacity during our previous study on monodisperse melts.[25] In that case, careful consideration of finite-size effects showed that the gyroid phase was actually the preferred morphology. The gyroid structure is particularly difficult to form due to its relatively large unit cell, which must be commensurate with the size of the simulation box.[33] If this condition is not met, the metastable PL phase generally occurs in its place.

Gyroid Phase with Monodisperse Matrix. To test for the gyroid (G) phase at $(N_A)_n$ = 13 and 14, we first estimated the preferred size of its unit cell from the peak in the disordered-state structure function to be $L \approx 50$. Given that, we ran a series of simulations in boxes of L = 48, 50, and 52 for an equilibration period of 4×10^6 MCS per monomer. G-like structures

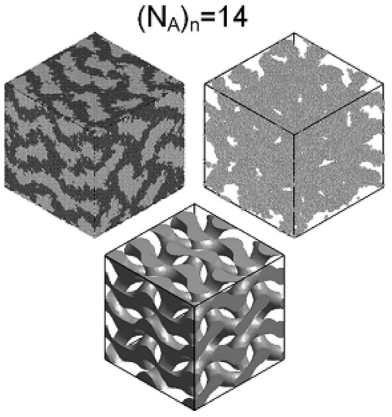

Figure 10. Gyroid (G) morphology at $(N_A)_n$ = 14 and χN = 51 from a simulation box of L = 100. The left image displays all the monomers while the right image only plots A-type monomers with 9 or more A-type neighbors. The bottom diagram compares a level-surface constructed from the $\sqrt{6}$ and $\sqrt{8}$ basis functions of the *Ia*3*d* space-group symmetry.

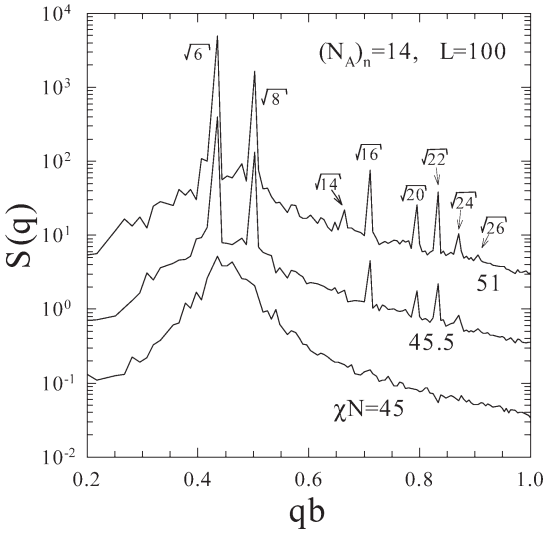

Figure 11. Spherically averaged structure function, $S(q)$, of the gyroid (G) phase at $(N_A)_n$ = 14 and L = 100, showing the disappearance of high-order reflections with decreasing χN. For clarity, the bottom two curves have been shifted downward by 1 and 2 decades.

spontaneously formed in the L = 50 box, but the L = 48 and 52 boxes both produced a mixture of PL- and G-like morphologies populated with numerous defects.

Unlike for the monodisperse system,[25] here the G phase produced clear spikes in the heat capacity, as shown in Figure 9. The distinctive spike for $(N_A)_n$ = 13 suggests that G is the true equilibrium phase, since the transition to PL was not strong enough to produce one at that composition. For $(N_A)_n$ = 14, on the other hand, the C_V spike from G occurred at a slightly higher value of χN = 44 than the one from PL at χN = 43.3, suggesting that PL is slightly more stable than G. However, this difference is within the statistical inaccuracy characteristic of our simulations.[25] In any case, the competition between PL and G is clearly much closer than it was in our previous study of monodisperse melts.

To confirm that the ordered phase is actually gyroid, some of the configurations were periodically repeated to fill boxes of

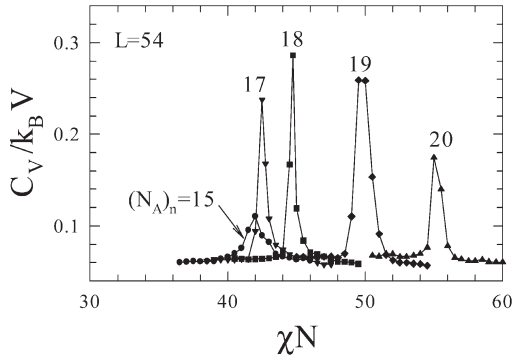

Figure 12. Heat capacity plots analogous to those in Figure 2, but for compositions exhibiting an ordered lamellar (L) phase.

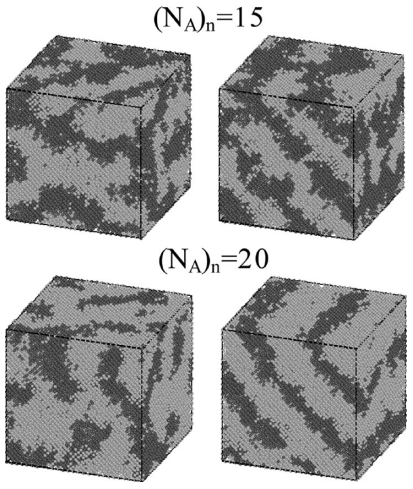

Figure 13. Configurations adjacent to the ODT at $(N_A)_n = 15$ ($\chi N = 41.5$ and 42.5) and $(N_A)_n = 20$ ($\chi N = 54.5$ and 55.5) demonstrating transitions to the lamellar (L) phase.

$L = 100$ and then equilibrated for a further 10^6 MCS per monomer. Figure 10 shows the resulting configuration for $(N_A)_n = 14$ at $\chi N = 51$, plotted first with all monomers and then with just the A-type monomers that have at least 9 A-type neighbors. The Monte Carlo configuration is also compared to a level surface, generated from a linear combination of the $\sqrt{6}$ and $\sqrt{8}$ basis functions of the *Ia*3*d* space group to approximate the A/B interface of the G morphology. The resemblance is rather striking. Further confirmation of the *Ia*3*d* symmetry comes from the spherically averaged structure function, $S(q)$, plotted in Figure 11. The appearance of the first 8 *Ia*3*d* peaks leaves no doubt that the ordered phase is indeed gyroid. Analogous results were obtained for $(N_A)_n = 13$.

The heat capacity spikes in Figure 9 are obtained from just a single unit cell of G, and so we also located the ODT from the larger simulation box, $L = 100$, by examining the disappearance of the peaks in $S(q)$. Following the same procedure as for the fcc spheres, an ordered morphology is equilibrated at a series of higher temperatures for 10^6 MCS per monomer (without parallel tempering swaps). According to $S(q)$, the G phase appears to disorder at $\chi N = 45$ for $(N_A)_n = 14$, as illustrated in Figure 11, and at $\chi N = 45.5$ for $(N_A)_n = 13$. These values are slightly higher than those obtained from the spike in C_V, which is not too surprising since a larger simulation box permits more fluctuations. Given

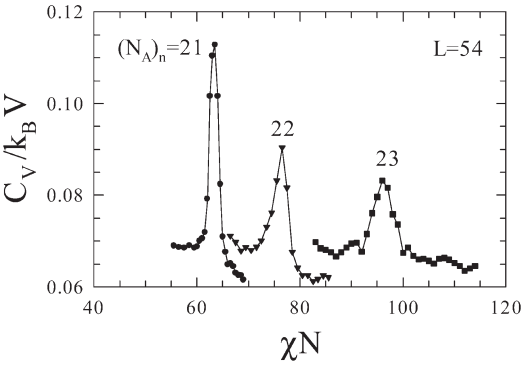

Figure 14. Heat capacity plots analogous to those in Figure 2, but for simulations exhibiting an ordered perforated-lamellar (PL) phase.

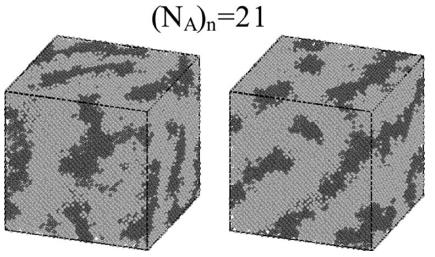

Figure 15. Configurations adjacent to the ODT ($\chi N = 63$ and 64) at $(N_A)_n = 21$ demonstrating a transition to the inverted perforated-lamellar (PL) phase.

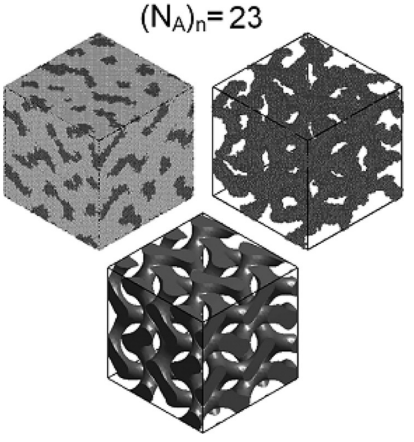

Figure 16. Analogous to Figure 10, but showing an inverted gyroid (G) morphology at $(N_A)_n = 23$ and $\chi N = 103$ from a simulation box of $L = 96$.

that the bigger box is closer to the thermodynamic limit, these latter results are taken to be our best estimates of $(\chi N)_{ODT}$.

Lamellar Phase. The simple lamellar (L) phase was observed over the range of compositions $(N_A)_n = 15-20$. As Figure 12 shows, the ODT is readily identified by sizable spikes in the heat capacity; the $(N_A)_n = 16$ spike has been removed for the purpose of clarity. With the exception of $(N_A)_n = 15$, the spikes are roughly 3 times larger than any of those encountered so far. Further confirmation of the first-order transition comes from the fact that there is an abrupt change in morphology from one side of a spike to the other, as illustrated in Figure 13 for $(N_A)_n = 15$ and 20.

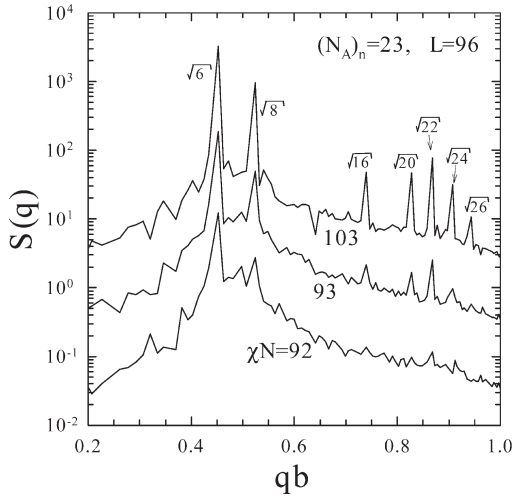

Figure 17. Analogous to Figure 11, but showing the disappearance of the high-order reflections from an inverted gyroid (G) morphology at $(N_A)_n = 23$ and $L = 96$.

The ordered configurations from $(N_A)_n = 16$ to 20 are clearly lamellar, with well-formed alternating A- and B-rich layers. However, the A-rich lamellae of the $(N_A)_n = 15$ configuration exhibit a small population of perforations, as previously encountered in the L phase of monodisperse melts.[23] These perforations are much different than the permanent densely packed ones in the PL morphology. In this case, the perforations are transient features that diffuse around the lamellae for just a few thousand MCS per monomer before closing up. We suspect that it is their presence that causes the peak in C_V to be significantly smaller than for the other compositions.

Perforated-Lamellar Phase with Polydisperse Matrix. In the standard box size of $L = 54$, an inverted PL phase with perforations in the monodisperse B-rich lamellae forms at compositions of $(N_A)_n = 21-23$. This time, the heat capacity plotted in Figure 14 displays clear spikes identifying the ODT. Although the spikes become smaller and broader with increasing $(N_A)_n$, they remain as large as for any of the nonlamellar phases. The C_V spikes are also accompanied by abrupt changes in the morphology, as illustrated in Figure 15 for $(N_A)_n = 21$. Unlike for the neighboring L phase at $(N_A)_n = 20$, the perforations are densely packed and permanent, at least, on the time scale of the simulations (i.e., 3×10^6 MCS per monomer). However, as with all instances of PL, we need to consider its potential metastability with respect to the G phase.

Gyroid Phase with Polydisperse Matrix. The peak in the disordered-state structure function at compositions $(N_A)_n = 21-23$ indicates a preferred size of $L \approx 46$ for the gyroid unit cell. Therefore, we investigated the range of box sizes, $L = 42$, 44, 46, 48, and 50. Even with a particularly long equilibration period of 5×10^6 MCS per monomer, G-like configurations only formed for the $(N_A)_n = 23$ composition. There were a few replicas in the $L = 46$ simulation box that exhibited G-like order, but they were defect-ridden. Some better formed G-like structures were produced in the $L = 48$ box, but even still they were intermixed with replicas exhibiting PL-like morphologies. The system evidently has considerable difficulty in choosing between the G and PL phases.

To test the stability of the G phase more thoroughly, we took one of the ordered configurations from the $L = 48$ simulation box for further investigation. It was periodically repeated to fill an $L = 96$ box and equilibrated for an additional 10^6 MCS per monomer at $\chi N = 103$. Figure 16 displays the resulting configuration plotted showing all the monomers and then again with just the B-type monomers possessing 6 or more B-type neighbors. As before, the configuration is compared to a level surface that approximates the A/B interface of the G morphology. The impressive similarity between the Monte Carlo configuration and the level surface strongly suggests that the G phase has been adopted.

The *Ia*3*d* symmetry of the configuration is further supported by the spherically averaged structure function, $S(q)$, plotted in Figure 17. Apart from the absence of a $\sqrt{14}$ peak, $S(q)$ exhibits the expected reflections for the G morphology. To identify the ODT, we then subjected the ordered configuration to 10^6 MCS per monomer at a series of higher temperatures (without parallel tempering swaps). The disappearance of the scattering peaks in Figure 17 indicates that the G phase disorders at about $(\chi N)_{ODT} = 92$. This is at a significantly lower segregation than the position of the heat capacity peak in Figure 14 at $\chi N = 96$, implying that G is more stable than PL for $(N_A)_n = 23$.

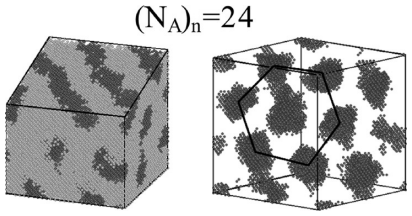

Figure 18. Ordered configuration at $(N_A)_n = 24$ and $\chi N = 117$. The left image is clipped to expose the cylindrical (C) morphology, while the right image shows the A-rich cylinders end-on revealing the approximate hexagonal packing.

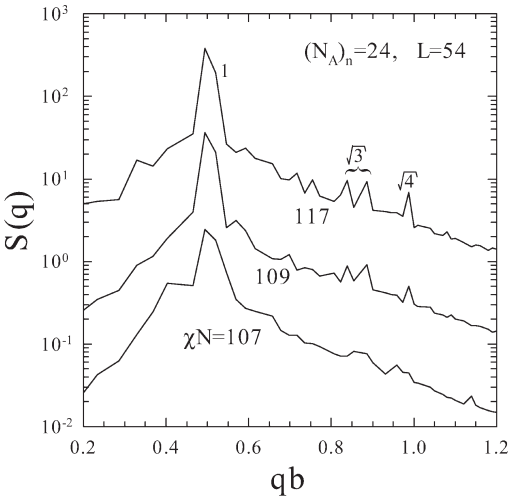

Figure 19. Analogous to Figure 11, but showing the disappearance of the high-order reflections from an inverted cylinder (C) morphology at $(N_A)_n = 24$ and $L = 54$.

Cylinder Phase with Polydisperse Matrix. At the largest compositions investigated, $(N_A)_n = 24$ and 25, ordered morphologies were particularly difficult to observe. After performing a total of 10^7 MCS per monomer over a wide range of segregations, the parallel tempering scheme only produced four ordered morphologies at $(N_A)_n = 24$ dispersed among defect-ridden

Table 1. Scattering Vectors, $\mathbf{q} = (h,k,l)/d$, Responsible for Peaks in the Structure Function, $S(\mathbf{q})$, for the Cylinder (C) Morphology Produced at $(N_A)_n = 24$ and $\chi N = 117$ in an $L = 54$ Simulation Box

hex peaks	$\mathbf{q}_1$	$\mathbf{q}_2$	$\mathbf{q}_3$
1	(2, −2, −1)	(1, −2, 2)	(1, 0, −3)
$\sqrt{3}$	(3, −4, 1)	(0, 2, −5)	(3, −2, −4)
$\sqrt{4}$	(4, −4, −2)	(2, −4, 4)	(2, 0, −6)

Table 2. Position of the ODT and the Ordered Morphology Obtained from Monte Carlo Simulations on $N = 30$ Diblocks at Various Compositions, $(N_A)_n$, for Polydisperse ($PDI_A = 1.5$) and Monodisperse ($PDI_A = 1.0$)[25] Melts

	polydisperse		monodisperse	
$(N_A)_n$	$(\chi N)_{ODT}$	phase	$(\chi N)_{ODT}$	phase
4	120.0	S	152.0	C
5	90.0	S	109.5	C
6	81.0	S	84.0	C
7			69.5	C
8	61.0	C	62.5	C
9	50.5	C	59.0	G
10	46.3	C	55.0	G
11	44.0	C	51.0	PL
12	44.0	C	46.0	L
13	46.0	PL/G	42.8	L
14	45.5	PL/G	41.0	L
15	42.0	L	40.5	L
16	42.0	L	41.0	L
17	42.5	L	42.8	L
18	44.8	L	46.0	L
19	48.5	L	51.0	PL
20	55.0	L	55.0	G
21	63.5	PL	59.0	G
22	76.5	PL	62.5	C
23	92.0	G	69.5	C
24	108.0	C	84.0	C
25	127.0	C	109.5	C

configurations and three at $(N_A)_n = 25$. Figure 18 displays one of the ordered configurations from $(N_A)_n = 24$ at $\chi N = 117$. In the left image, the simulation box has been clipped to show the internal structure of the phase which is clearly cylindrical, and in the right image, the matrix has been removed with the box oriented to display the approximate hexagonal packing of the cylinders.

Because of the exceptionally long equilibration times required to produce ordered configurations, the ODT could not be determined from the heat capacity. Therefore, we turned to the same method used for the fcc spherical and gyroid phases, where the transition was detected via the structure function, $S(q)$. At each composition, an ordered C configuration was subjected to 10^7 MCS per monomer of equilibration over a broad range of segregations (without parallel tempering swaps), and the ODT was identified by the loss of peaks in $S(q)$. In this case, the $L = 54$ box was considered to be large enough that we did not double its

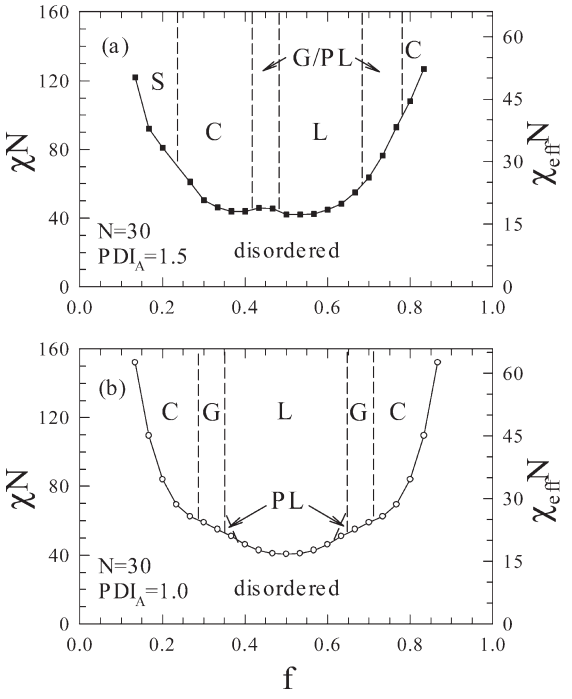

Figure 20. Monte Carlo phase diagrams for (a) polydisperse and (b) monodisperse[25] diblock copolymers of $N = 30$. The ordered phases are lamellar (L), perforated-lamellar (PL), gyroid (G), cylindrical (C), and spherical (S). The scale on the left axis is in terms of the lattice-based interaction parameter from eq 1, and the one on the right involves the effective parameter defined in eq 5.

dimensions. For $(N_A)_n = 24$, the peaks in $S(q)$ vanish at about $(\chi N)_{ODT} = 108$, as illustrated in Figure 19, and for $(N_A)_n = 25$, they disappear around $(\chi N)_{ODT} = 127$.

The scattering peaks in Figure 19 are significantly affected by the distortion of the hexagonal packing shown in Figure 18. Normally, each peak in $S(q)$ is made up of six contributions from three pairs of reflections, but this degeneracy is broken when the hexagonal unit cell becomes distorted. Table 1 lists the actual positions of the reflections in 3-dimensional reciprocal space ($\pm\mathbf{q}_i$, for $i = 1, 2, 3$) corresponding to the usual 1, $\sqrt{3}$, and $\sqrt{4}$ hexagonal peaks. In this particular case, the principal peak is spread over two neighboring values of $qd = (h^2 + k^2 + l^2)^{1/2} = \sqrt{9}$ and $\sqrt{10}$, producing a broad peak in Figure 19. (Recall that the lattice constant, d, is related to the bond length, b, by $b = \sqrt{2}d$.) The $\sqrt{3}$ hexagonal peak actually splits into two distinct peaks at $qd = \sqrt{26}$ and $\sqrt{29}$. The $\sqrt{4}$ hexagonal peak also splits into two distinct peaks at $qd = \sqrt{36}$ and $\sqrt{40}$, but the latter becomes obscured from spherical averaging it with the statistical noise.

Phase Diagram. Table 2 compiles the value of $(\chi N)_{ODT}$ and specifies the morphology of the ordered phase at each composition, $f = (N_A)_n/N$, investigated in our Monte Carlo study. The one exception is for $(N_A)_n = 7$, where we were unable to generate an ordered phase presumably because of the close proximity to the S/C phase boundary. For comparison purposes, Table 2 also includes the analogous results from our earlier study on monodisperse melts.[25]

The data in Table 2 is then used to construct the phase diagrams in Figure 20. The numerical accuracy of the ODT is about one or two units of χN, which roughly corresponds to the size of the symbols used to plot $(\chi N)_{ODT}$. The OOTs are shown schematically as vertical dashed lines positioned so as to coincide

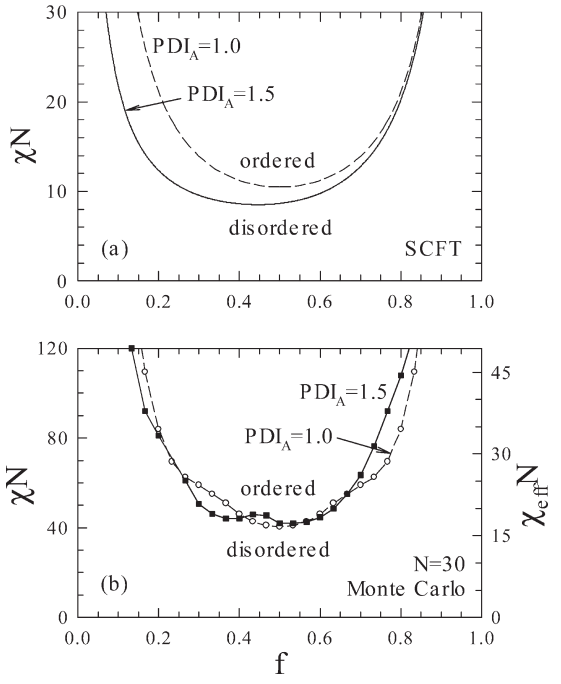

Figure 21. Order−disorder transitions (ODTs) for polydisperse (solid curves) and monodisperse (dash curves) melts as predicted by (a) SCFT[18] and (b) Monte Carlo simulations.

with the morphologies listed in Table 2. The left axis is labeled in terms of the lattice-based χ parameter defined in eq 1, which differs from the more common definition used by the continuum model of SCFT. In order to facilitate quantitative comparison with SCFT,[18] the right axis is labeled with an effective interaction parameter[34,35]

$$\chi_{\text{eff}} \equiv \frac{z_{\text{eff}}\varepsilon_{\text{AB}}}{k_{\text{B}}T} \tag{5}$$

where the effective coordination number, $z_{\text{eff}} = 4.94$, was evaluated previously[25] from the number of intermolecular contacts in an athermal melt ($\chi = 0$) extrapolated to infinite N.

Interestingly, the ODT of the polydisperse system exhibits a noticeable bump at the complex phase window, $f \approx 0.45$ (see Figure 20a). This feature has been observed in experiments on monodisperse melts,[36,37] but this is the first time it has been seen in simulations. It implies that the microstructure of the complex phases is more easily disrupted by thermal fluctuations than that of the neighboring lamellar and cylindrical phases. This may in part be due to the polydispersity of A-type blocks making up the minority component networks, but it may also have something to do with the location of the complex phase window. The effect could be more pronounced than usual due to the fact that the slope of the ODT is relatively flat.

The most striking effect of polydispersity is the shift in the OOTs toward larger A-block composition, f. There was some evidence of this in our previous Monte Carlo study[23] at $f = 0.5$, where the lamellar phase became perforated at large PDI_A, but the effect is much clearer in the full phase diagrams of Figure 20. This result is qualitatively consistent with both experiment[11−14] and SCFT[15,16,18] and is readily explained by the fact that polydispersity reduces the entropic stretching energy of the A-rich domains.

Nevertheless, the principal aim of this study was to resolve the discrepancy between the Lynd−Hillmyer experiments[12] and the SCFT prediction[18] regarding the effect of polydispersity on the ODT. As illustrated in Figure 21a, SCFT predicts that polydispersity lowers $(\chi N)_{\text{ODT}}$ over the entire range of compositions, f. Although experiments also found a decrease in $(\chi N)_{\text{ODT}}$ when the minority domains were polydisperse (i.e., small f), they instead observed an increase in $(\chi N)_{\text{ODT}}$ when the matrix was polydisperse (i.e., large f). Indeed, the comparison in Figure 21b of our ODT for polydisperse melts with that for the monodisperse melts[25] shows a decrease in $(\chi N)_{\text{ODT}}$ for $f \lesssim 0.4$ and an increase in $(\chi N)_{\text{ODT}}$ for $f \gtrsim 0.7$. Between these compositions, the ODTs are indistinguishable within our statistical accuracy apart from the small rise in $(\chi N)_{\text{ODT}}$ for $0.4 \lesssim f \lesssim 0.5$, which we attributed to the complex phase window of the polydisperse system. This effect may have just been too subtle for the experiments to capture. (It is very difficult to synthesize monodisperse and polydisperse diblocks with the same average molecular weight and composition.) There is also a region at small f where the two ODTs come quite close to each other again, but this is below the compositions examined by the experiments and also a region where macrophase separation may become important; we will have more to say about this in the Discussion. All things considered, there is good qualitative agreement between the simulations and the experiments.

DISCUSSION

The fact that our Monte Carlo simulations bring the behavior of the ODT into agreement with experiment implies that polydispersity has an important effect on composition fluctuations, since this is what SCFT overlooks. The standard fluctuation correction to the mean-field ODT, developed by Fredrickson and Helfand,[38] predicts an upward shift in $(\chi N)_{\text{ODT}}$ proportional to $\overline{N}^{-1/3}$, where $\overline{N} = a^6\nu^{-2}N$ is the invariant polymerization index, a is the statistical segment length, and ν is the segment volume. The simplest explanation for the contrary results in Figure 21 is that the amplitude of the fluctuation-induced correction is greater for polydisperse melts than for monodisperse melts, sufficiently so as to counteract the reduction in $(\chi N)_{\text{ODT}}$ predicted by SCFT in Figure 21a. The Fredrickson−Helfand correction has not yet been applied to the present model, but Burger and Semenov[39] have applied it to diblocks with equal polydispersity in both blocks. However, polydispersity still produced a substantial decrease in $(\chi N)_{\text{ODT}}$ over the full range of compositions, and it is likely that the same would remain true if only one block was polydisperse. Notably there are developments[40,41] underway to improve upon the fluctuation correction of Fredrickson and Helfand, and this may bring the theory into better agreement with experiment.

An important consideration, though, is that the experiments as well as our simulations involve values of $\overline{N}$ far below the applicability of the Fredrickson−Helfand treatment.[38] Fredrickson and Helfand stated that the assumptions in their theory are only strictly valid for $\overline{N} \gtrsim 10^{10}$; their justification for applying them to smaller values is simply that the calculation continues to predict sensible phase diagrams for $\overline{N} \gtrsim 10^4$. Even still, this invariant polymerization index is large relative to the Lynd−Hillmyer experiments,[12] where $\overline{N} \approx 1200$ for their poly(styrene)−poly(isoprene) diblocks and $\overline{N} \approx 300$ for their poly(ethylene-*alt*-propylene)−poly(DL-lactide) diblocks. In our simulations, the invariant polymerization is just $\overline{N} \approx 100$.[24]

One of the Fredrickson−Helfand assumptions, which certainly no longer holds, is that the melt remains weakly segregated at the ODT. In reality, the centers of the A- and B-rich domains in our simulations are relatively pure. We suspect that at this level of segregation there are now important effects beyond what a weak-segregation approach can account for, such as packing frustration.[42] Indeed, a completely different theoretical approach may be required for these values of $\overline{N}$, even for monodisperse melts.

Polydispersity relieves packing frustration in the A-rich domains due to the reduction in entropic stretching energy and in the B-rich domains due to diblocks that detach from the interface on account of their small A blocks.[17] As previously pointed out,[23] this weakens the tendency for domains to order, which in turn allows composition fluctuations to have a larger effect causing a general upward shift in $(\chi N)_{ODT}$. The reduced tendency to order also accounts for the increased difficulty we experienced in trying to detect the ODT, relative to our earlier study[25] on monodisperse melts.

Packing frustration is also attributed to creating a preference for G over PL.[42,43] Consistent with a reduction in packing frustration, the competition between G and PL is much closer than for the monodisperse melts, where G survives to significantly higher χN than PL provided that the simulation box is commensurate with the preferred size of its unit cell. The situation is quite different for the polydisperse melts. On the left side of the phase diagram at $(N_A)_n = 13$ and 14, there is no longer a discernible difference in the ODTs for PL and G. It is only the fact that G is able to displace PL in the $L = 50$ simulation box that suggests G is the true equilibrium phase. On the other side of the diagram, G does survive fluctuations to a significantly lower χN than PL for $(N_A)_n = 23$. However, there are two compositions, $(N_A)_n = 21$ and 22, next to the L region where PL formed and G did not despite examining five separate system sizes centered about the expected size of its unit cell. Consistent with this, Lynd and Hillmyer[12] did find one sample on this side of the phase diagram exhibiting the PL morphology. Listak et al.[13] also observed PL, but on the other side of the phase diagram; notably their polydispersity was higher, their molecular-weight distribution was significantly less skewed, and there was a modest amount of homopolymer in their samples.

The two-phase coexistence regions predicted by SCFT[18] and observed in some experiments[9,10,21,22] were absent in our simulations. Basic thermodynamics predicts these regions to emerge along each of the phase boundaries, due to the fact that the competing phases have a preference for different portions of the molecular weight distribution (e.g., the lamellar phase favors the more symmetric diblocks while the other phases prefer the asymmetric molecules to varying degrees). It therefore becomes energetically favorable for the molecular-weight distribution to fractionate into two populations, one for each of the coexisting phases. However, macrophase separation requires the transport of material over macroscopic distances, and thus the equilibration time for this can become prohibitive. This applies to both simulations and experiments. In simulations, though, there is a more serious impediment to macrophase separation—the energy cost of forming an interface between the coexisting phases. The system size has to be rather large before the energy gain from macrophase separation is able to compensate for the penalty of forming the interface. If we were dealing with just a binary blend (i.e., two separate molecular weights), then we might overcome this problem by performing simulations in the grand-canonical ensemble. However, this is inconceivable when our polydisperse system contains on the order of 100 separate molecular weights (see Figure 1), each of which requires a separate chemical potential.

Nevertheless, the two-phase regions should still be relatively narrow for $PDI_A = 1.5$ according to SCFT,[18] with perhaps the exception of the one separating the disordered phase from the ordered spheres at small f. For sufficiently asymmetric compositions, the disordered phase will start to form spherical micelles as the temperature is reduced, predominantly from the diblocks with the longer A blocks. At some point, the spheres will start to aggregate into a close-packed arrangement (most certainly in an imperfect lattice which is neither fcc nor hcp), leading to coexistence between a spherical and a disordered phase. As the temperature is reduced further, the spheres will start to incorporate diblocks with ever shorter A blocks, causing the disordered phase to shrink away until only a spherical phase remains. Unfortunately, Lynd and Hillmyer did not consider sufficiently small compositions, f, to produce spheres, as it would have been interesting to see if experiments could actually detect this behavior.

SUMMARY

Using lattice-based Monte Carlo simulations, a phase diagram was generated for melts of AB diblock copolymer composed of polydisperse A blocks joined to monodisperse B blocks (see Figure 20a). Although the simulations were performed in the canonical ensemble, which prevents the formation of two-phase coexistence, our study was restricted to a moderate A-block polydispersity index of $PDI_A = (N_A)_w/(N_A)_n = 1.5$ for which these regions are expected to be narrow.[18] We also chose a fixed number-averaged polymerization of $N = (N_A)_n + N_B = 30$ (corresponding to an invariant polymerization index of $\overline{N} \approx 100$) to match that of our previous phase diagram for monodisperse melts (see Figure 20b)[25] so as to allow for direct comparison. The polydispersity caused a sizable shift in the order−order transitions (OOTs) toward higher A-monomer compositions, $f = (N_A)_n/N$, as previously predicted by self-consistent field theory (SCFT)[15,16,18] and observed in experiment.[11−14] However, unlike the SCFT, which predicts the order−disorder transition (ODT) to shift toward lower segregations at all compositions (see Figure 21a), the Monte Carlo simulations observe a reduction in $(\chi N)_{ODT}$ for small f and an increase in $(\chi N)_{ODT}$ for large f (see Figure 21b). This is in good agreement with the experiments of Lynd and Hillmyer.[12]

This difference between SCFT and the simulations implies that polydispersity increases the fluctuation-induced shift of the mean-field ODT. We attribute this to a reduction in packing frustration, which in turn weakens the tendency of domains to order into a regular periodic structure. Indeed, it was generally more difficult to detect the ODT in the polydisperse as opposed to the monodisperse melts. The reduced packing frustration also explains the closer competition between the complex G and PL structures, which evidently leads to a stable PL region between L and G on the large-f side of the phase diagram as observed by Lynd and Hillmyer.[12]

AUTHOR INFORMATION

Corresponding Author

*E-mail: T.M.Beardsley@reading.ac.uk (T.M.B.); M.W.Matsen@reading.ac.uk (M.W.M.).

■ ACKNOWLEDGMENT

We have benefited from useful discussions with Patrick Fairclough, Marc Hillmyer, Nate Lynd, and Rob Wickham. This work was supported by the EPSRC (EP/E010342/1).

■ REFERENCES

(1) Bates, F. S.; Fredrickson, G. H. *Phys. Today* **1999**, *52*, 32–38.
(2) Bates, F. S.; Schulz, M. F.; Khandpur, A. K.; Förster, S.; Rosedale, J. H.; Almdal, K.; Mortensen, K. *Faraday Discuss.* **1994**, *98*, 7–18.
(3) Schulz, M. F.; Bates, F. S.; Almdal, K.; Mortensen, K. *Phys. Rev. Lett.* **1994**, *73*, 86–89.
(4) Hajduk, D. A.; Harper, P. E.; Gruner, S. M.; Honeker, C. C.; Kim, G.; Thomas, E. L.; Fetters, L. J. *Macromolecules* **1994**, *27*, 4063–4075.
(5) Hamley, I. W.; Koppi, K. A.; Rosedale, J. H.; Bates, F. S.; Almdal, K.; Mortensen, K. *Macromolecules* **1993**, *26*, 5959–5970.
(6) Hajduk, D. A.; Takenouchi, H.; Hillmyer, M. A.; Bates, F. S.; Vigild, M. E.; Almdal, K. *Macromolecules* **1997**, *30*, 3788–3795.
(7) Takenaka, M.; Wakada, T.; Akasaka, S.; Nishitsuji, S.; Saijo, K.; Shimizu, H.; Kim, M. I.; Hasegawa, H. *Macromolecules* **2007**, *40*, 4399–4402.
(8) Hillmyer, M. A. *J. Polym. Sci., Part B* **2007**, *45*, 3249–3251.
(9) Bendejacq, D.; Ponsinet, V.; Joanicot, M.; Loo, Y.-L.; Register, R. A. *Macromolecules* **2002**, *35*, 6645–6649.
(10) Lynd, N. A.; Hamilton, B. D.; Hillmyer, M. A. *J. Polym. Sci., Part B* **2007**, *45*, 3386–3393; the two macrophase-separated samples are consistent with L + C coexistence (private communication).
(11) Lynd, N. A.; Hillmyer, M. A. *Macromolecules* **2005**, *38*, 8803–8810.
(12) Lynd, N. A.; Hillmyer, M. A. *Macromolecules* **2007**, *40*, 8050–8055.
(13) Listak, J.; Jakubowski, W.; Mueller, L.; Plichta, A.; Matyjaszewski, K.; Bockstaller, M. R. *Macromolecules* **2008**, *41*, 5919–5927.
(14) Ruzette, A.-V.; Tence-Girault, S.; Leibler, L.; Chauvin, F.; Bertin, D.; Guerret, O.; Gerard, P. *Macromolecules* **2006**, *39*, 5804–5814.
(15) Sides, S. W.; Fredrickson, G. H. *J. Chem. Phys.* **2004**, *121*, 4974–4986.
(16) Cooke, D. M.; Shi, A.-C. *Macromolecules* **2006**, *39*, 6661–6671.
(17) Matsen, M. W. *Eur. Phys. J. E* **2006**, *21*, 199–207.
(18) Matsen, M. W. *Phys. Rev. Lett.* **2007**, *99*, 148304.
(19) Semenov, A. E. *Sov. Phys. JETP* **1985**, *61*, 733–742.
(20) Matsen, M. W.; Bates, F. S. *J. Chem. Phys.* **1997**, *106*, 2436–2448.
(21) Matsushita, Y.; Noro, A.; Iinuma, M.; Suzuki, J.; Ohtani, H.; Takano, A. *Macromolecules* **2003**, *36*, 8074–8077.
(22) Noro, A.; Iinuma, M.; Suzuki, J.; Takano, A.; Matsushita, Y. *Macromolecules* **2004**, *37*, 3804–3808.
(23) Beardsley, T. M.; Matsen, M. W. *Eur. Phys. J. E* **2008**, *27*, 323–333.
(24) Vassiliev, O. N.; Matsen, M. W. *J. Chem. Phys.* **2003**, *118*, 7700–7713.
(25) Beardsley, T. M.; Matsen, M. W. *Eur. Phys. J. E* **2010**, *32*, 255–264.
(26) Geyer, C. J.; Thompson, E. A. *J. Am. Stat. Assoc.* **1995**, *90*, 909–920.
(27) Hukushima, K.; Nemoto, K. *J. Phys. Soc. Jpn.* **1996**, *65*, 1604–1608.
(28) Earl, D. J.; Deem, M. W. *Phys. Chem. Chem. Phys.* **2005**, *7*, 3910–3916.
(29) Lee, J. Y.; Kosterlitz, J. M. *Phys. Rev. B* **1991**, *43*, 3265–3277.
(30) Lynd, N. A.; Hillmyer, M. A.; Matsen, M. W. *Macromolecules* **2008**, *41*, 4531–4533.
(31) Schultz, G. V. *Z. Phys. Chem. (Munich)* **1939**, *B43*, 25–46.
(32) Zimm, B. H. *J. Chem. Phys.* **1948**, *16*, 1099–1116.
(33) Martinez-Veracoechea, F.; Escobedo, F. A. *Macromolecules* **2005**, *38*, 8522–8531.
(34) Müller, M.; Binder, K. *Macromolecules* **1995**, *28*, 1825–1834.
(35) Morse, D. E.; Chung, J. K. *J. Chem. Phys.* **2009**, *130*, 224901.
(36) Khandpur, A. K.; Förster, S.; Bates, F. S.; Hamley, I. W.; Ryan, A. J.; Bras, W.; Almdal, K.; Mortensen, K. *Macromolecules* **1995**, *28*, 8796–8806.
(37) Schultz, M. F.; Khandpur, A. K.; Bates, F. S.; Almdal, K.; Mortensen, K.; Hajduk, D. A.; Gruner, S. M. *Macromolecules* **1996**, *29*, 2857–2867.
(38) Fredrickson, G. H.; Helfand, E. *J. Chem. Phys.* **1987**, *87*, 697–705.
(39) Burger, C.; Ruland, W.; Semenov, A. N. *Macromolecules* **1990**, *23*, 3339–3346. **1991**, *24*, 816.
(40) Grzywacz, P.; Qin, J.; Morse, D. C. *Phys. Rev. E* **2007**, *76*, 061802.
(41) Morse, D. C.; Qin, J. A. *J. Chem. Phys.* **2011**, *134*, 084902.
(42) Matsen, M. W.; Bates, F. S. *Macromolecules* **1997**, *29*, 7641–7644.
(43) Matsen, M. W. *J. Phys.: Condens. Matter* **2002**, *14*, R21–R47.